nature communications

Article

https://doi.org/10.1038/s41467-026-68666-z

Glycine photosynthesis via C–N coupling of waste plastic and nitrate over diatomic Pd–B catalyst

Received: 26 August 2025

Accepted: 12 January 2026

Published online: 20 January 2026

Check for updates

Zongyang Ya[1,2,8], Mei Li[3,8], Donglong Fu[1,8], Yu Zheng[2], Ruhan Wei[2], Hao Wang[2], Kangning Zhang[2], Dong Xu[1], Zixuan Zhang[1], Xue Zhang[1], Shen Yan[1], Hua Wang[1] ✉, Shengbo Zhang[1,2,4] ✉ & Jinlong Gong[1,5,6,7] ✉

Photocatalytic C–N coupling offers a promising approach for the sustainable production of amino acids, but the uncontrolled coupling pathway of reaction intermediates limits yield and selectivity. This paper describes a Pd–B diatomic catalyst that can selectively catalyze the photosynthesis of glycine via C–N coupling reaction between waste poly(ethylene terephthalate)-derived ethylene glycol and nitrate, achieving a glycine yield of 2.9 mmol g_{cat}^{-1} h^{-1} with a selectivity of 92%. Mechanistic investigations reveal that ethylene glycol is photo-oxidized to glycolaldehyde at the hole-rich B site, while nitrate is photo-reduced to NH_4^+/NH_3 at the electron-rich Pd site. Subsequently, glycolaldehyde undergoes C–N coupling with NH_4^+/NH_3, and further photo-oxidized to form glycine. The Pd–B diatomic site more effectively stabilizes the glycolaldehyde intermediate, resulting in a more favorable C–N coupling pathway than metal oxide and enhancing glycine selectivity. Thus, we show a catalytic system for selective glycine photosynthesis by precisely regulating the reaction pathways of key intermediates.

Glycine, the simplest α-amino acid in structure, serves not only as a fundamental unit in protein synthesis but also as an indispensable key material across diverse fields, including food, pharmaceutical, agricultural, and organic synthesis[1–4]. Currently, the global annual production of glycine has surpassed 740,000 tons[5], and the demand is exhibiting a steady growth trend with the continuous expansion of the pesticide, pharmaceutical and food industries[6]. However, conventional glycine synthesis methods, particularly the widely employed Strecker approach, are hindered by several significant limitations, such as the reliance on highly toxic cyanide-based reagents, harsh reaction conditions, and intricate synthetic pathways. These factors significantly impact the quality of glycine produced, as well as its production costs and environmental sustainability (Fig. 1a)[7–9]. Consequently, developing mild, efficient and sustainable pathways for glycine production holds substantial strategic importance for the rational utilization of energy resources and environmental protection.

The photocatalytic conversion of carbon-containing small molecules (such as CO_2, CH_4, or methanol) and nitrogen-containing substrates (such as N_2, or NH_3) into amides or amino acids via the C–N coupling reaction has emerged as a highly promising sustainable strategy because of its mild reaction and high atom economy[10–17]. In particular, polyols, acting as highly active photochemical reagents,

[1]School of Chemical Engineering & Technology, Key Laboratory for Green Chemical Technology of Ministry of Education, Tianjin University; Collaborative Innovation Center for Chemical Science & Engineering, Tianjin, China. [2]School of Environmental Science and Engineering, Tianjin Key Laboratory of Biomass/Wastes Utilization, Tianjin University, Tianjin, China. [3]School of Materials Science and Engineering, Smart Sensing Interdisciplinary Science Center, Nankai University, Tianjin, China. [4]Key Laboratory of Advanced Energy Materials Chemistry, Ministry of Education (Nankai University), Tianjin, China. [5]International Joint Laboratory of Low-carbon Chemical Engineering of Ministry of Education, Tianjin, China. [6]State Key Laboratory of Synthetic Biology, Tianjin University, Tianjin, China. [7]Tianjin Normal University, Tianjin, China. [8]These authors contributed equally: Zongyang Ya, Mei Li, Donglong Fu.
✉e-mail: tjuwanghua@tju.edu.cn; shengbozhang@tju.edu.cn; jlgong@tju.edu.cn

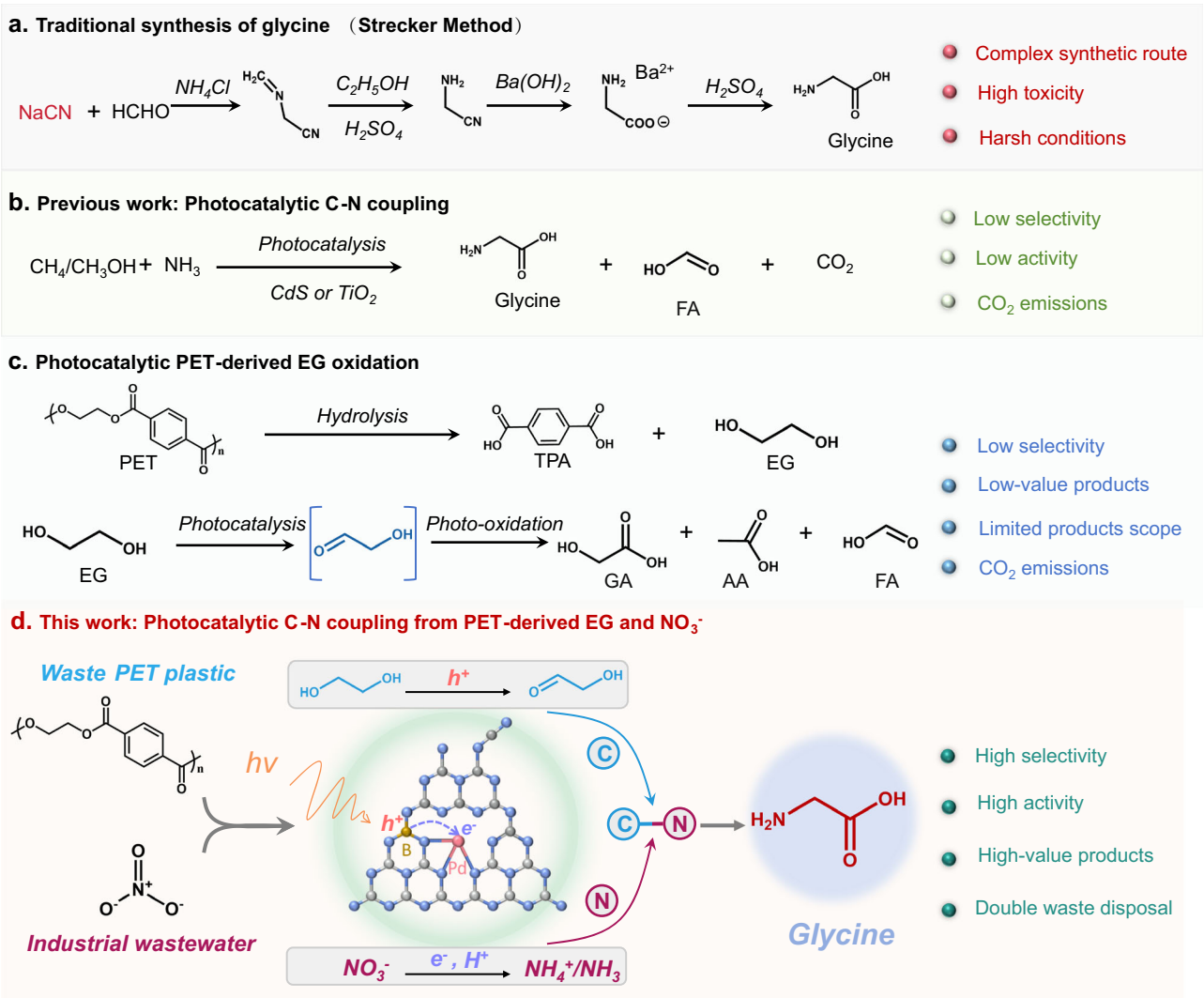

Fig. 1 | Schematic diagram. a Traditional Strecker method for the synthesis of glycine. **b** Previous work on C–N coupling of small molecules into glycine on semiconductor photocatalysts. **c** Photocatalytic PET-derived EG into glycolic acid (GA), acetic acid (AA) and formic acid (FA) products. **d** This work: selective photocatalytic synthesis of glycine from waste PET plastic and nitrate waste via C–N coupling reaction of key intermediates on a Pd–B diatomic catalyst. The blue sphere represents the N element, the gray sphere represents the C element, the brown sphere represents the B element, and the pink sphere represents the Pd element. These arrows represent conversion or formation.

have been established as renewable carbon precursors for amino acid synthesis. Specifically, the hydroxyl group (C–OH) in polyols can be photo-oxidized to generate electrophilic aldehyde groups (H–C=O)[13,18], which then react with nitrogen-containing nucleophiles to construct C–N bonds[13,18,19]. Compared with inert N_2 (946 kJ/mol), nitrate (NO_3^-) in wastewater serves as a more suitable nitrogen source for photocatalytic C–N bond formation due to its high polarity and low N=O bond dissociation energy (204 kJ/mol)[20,21]. To date, only a few rare active catalysts (TiO_2, CdS) have been reported for the photocatalytic synthesis of glycine via C–N coupling reaction from CH_4, CO_2, or methanol[2,10,11,14]. Nevertheless, despite these advances, the selectivity and yield of glycine remain unsatisfactory, primarily due to side reactions involving high-energy C–C coupling and the inevitable overoxidation process of key intermediates (electrophilic aldehydes) into organic acids or CO_2 terminal byproducts (Fig. 1b)[22,23]. These bottlenecks underscore the significance and challenge of designing a photocatalytic system capable of achieving selective C–N coupling to attain high yields of glycine.

Poly(ethylene terephthalate) (PET), as the most produced and widely consumed polyester plastic globally, boasts an annual output of approximately 100 million tons, primarily synthesized through the polymerization of terephthalic acid (TPA) and ethylene glycol (EG)[24]. However, over 80% of PET waste ends up in landfills or is discharged into the environment, posing a severe threat to ecosystems and resulting in significant carbon resource waste[25,26]. Chemical hydrolysis of PET into TPA and EG monomers is generally regarded as a highly promising recycling approach (Fig. 1c)[27,28]. Nevertheless, in practical implementation, the separation and purification of EG via distillation are operationally complex and costly due to its high boiling point (197.3 °C) and water solubility[29]. Moreover, given the relatively low market price of EG ($800 per ton) and its widespread availability, it is even less cost-effective to purify the hydrolyzed EG solution for reuse in PET production. Instead, photocatalytic oxidation of PET-derived EG into higher-value-added products, such as glycolic acid (GA, $20000 per ton) or acetic acid (AA, $3000 per ton), has emerged as a highly attractive alternative pathway (Fig. 1c)[30–33]. However, the significant challenge of this photocatalytic process is low selectivity and a limited product scope, primarily acids. Developing a strategy to expand the product range will help to reintroduce waste carbon from plastics into the utilization cycle[34]. Sufficient evidence has demonstrated that the

electrophilic glycolaldehyde serves as a key intermediate in the photooxidation of EG to form organic acids[32,35,36]. Therefore, developing a catalyst capable of effectively stabilizing and capturing electrophilic glycolaldehyde intermediates during EG photo-oxidation to achieve selective C–N coupling with nitrate for photosynthesis of high-value glycine ($4600 per ton) would be a highly promising and scientifically valuable research strategy.

Atomically dispersed catalysts, owing to their tuneable coordination environments and electronic structure, offer the possibility for the selective adsorption and activation of substrates or reaction intermediates[37,38]. In particular, diatomic catalysts featuring dual redox active sites demonstrate distinct advantages over single-atom catalysts in simultaneously enhancing photocatalytic redox activity and product selectivity[36,39–42]. Therefore, we hypothesize that constructing diatomic photocatalysts containing redox sites could simultaneously strengthen the selective adsorption and activation of EG and NO_3^-, thereby achieving both high efficiency and selectivity in the photocatalytic synthesis of glycine. To verify the above hypothesis, we develop an efficient glycine photosynthesis route via C–N coupling of waste PET-derived EG and NO_3^- over a Pd–B diatomic catalyst (Fig. 1d). Mechanistic analysis shows that the key intermediates in glycine photosynthesis include an electrophilic glycolaldehyde generated via the photocatalytic oxidation of EG at the hole-rich B sites, and NH_4^+/NH_3 produced through the photocatalytic reduction of NO_3^- at the electron-rich Pd sites. Subsequently, the C–N coupling between glycolaldehyde and NH_4^+/NH_3 yields ethanolamine, which is further photo-oxidized to glycine. In this process, the Pd–B diatomic site is more conducive to stabilizing the glycolaldehyde intermediate to complete the C–N coupling pathway and avoid deep oxidation to organic acids compared to metal oxide catalysts, resulting in a high selectivity for glycine (> 92%). Furthermore, the strong electronic interaction between the Pd–B diatomic sites enhances light absorption and photoelectron transfer dynamics, thereby facilitating the efficient photosynthesis of glycine, with a generation rate of 2.9 mmol g_{cat}^{-1} h^{-1}. This process has been successfully scaled up to the gram level, enabling the conversion of real-world PET plastic waste and biomass-derived polyols into glycine using natural sunlight.

Results

Catalyst synthesis and characterization

B-doped carbon nitride-anchored Pd single-atom catalyst (Pd SA/BCNx) was synthesized according to our previously reported procedure with minor modifications (see methods)[36]. Transmission electron microscopy (TEM) images reveal that the Pd SA/BCNx catalyst possesses a hollow nanotube morphology with an average diameter of 550 ± 20 nm and an average wall thickness of 110 ± 5 nm (Fig. 2a). High-resolution transmission electron microscopy (HR-TEM) image confirms the absence of discernible metal or metal oxide nanoparticles within the catalyst (Fig. 2b). Aberration-corrected high-angle annular dark field-scanning transmission electron microscopy (AC-HAADF-STEM) shows numerous bright spots scattered on the nanotube (Fig. 2c), providing direct evidence for the atomically dispersed state of palladium on the support. Furthermore, energy-dispersive X-ray spectroscopy (EDS) elemental mapping images clearly reveal the uniform distributions of B, C, N, and Pd on the carbon nitride nanotubes (Fig. 2d).

The crystal phase and molecular structure of the catalysts were further identified through X-ray diffraction (XRD) patterns, Fourier transform infrared (FT-IR) spectroscopy and electron spin resonance (ESR) spectroscopy. The results indicate that the BCNx support retains the crystalline phase[43,44] and molecular structure of graphitic carbon nitride (g-C_3N_4), and successfully incorporates cyano groups (C≡N) into the molecular structure (Supplementary Fig. 1a–c)[45]. Furthermore, the solid-state ^{11}B NMR spectrum of Pd SA/BCNx precisely reveals that B atoms partially substituted the C-terminal positions of the triazine units and resided at the B1 site in Pd SA/BCNx (Supplementary Fig. 1d). The corresponding molecular structure is shown in the inset of Supplementary Fig. 1d, and the yellow ball indicated by the arrow represents the B1 position in Pd SA/BCNx. X-ray photoelectron spectroscopy (XPS) further confirms the chemical and oxidation states of C, N, B and Pd elements in Pd SA/BCNx, and the doping content of B and Pd is approximately 1.37 wt% and 1.04 wt%, respectively (Supplementary Fig. 2a–d and Supplementary Table 1). The doping content of B and Pd is also further determined through EDS elemental analysis (B:1.24 wt%; Pd:0.98 wt%) and inductively coupled plasma optical emission spectrometry (ICP-OES) (Pd:1.07 wt%). The B 1*s* spectrum of the BCNx sample exhibits a prominent peak at 191.9 eV, attributable to the B–N bond (Supplementary Fig. 2c)[36,46]. The Pd 3*d* spectrum shows two peaks at 342.9 eV and 337.6 eV in the B-free Pd SA/CN sample, corresponding to $Pd^{\delta+}$ $3d_{3/2}$ and $Pd^{\delta+}$ $3d_{5/2}$ ($0 < \delta < 2$), respectively (Supplementary Fig. 2d)[47,48]. Notably, compared with BCNx, the B–N bond peak in Pd SA/BCNx shifts to a higher binding energy by 0.2 eV, whereas the $Pd^{\delta+}$ peaks shift to a lower binding energy by 0.2 eV, suggesting a stronger electronic interaction between the atomic Pd site and the B site.

The local coordination environment and oxidation state of Pd single atoms in Pd SA/BCNx were further determined by X-ray absorption spectroscopy (XAS). The Pd *K*-edge X-ray absorption near-edge structure (XANES) spectra reveal that the absorption edges for Pd SA/BCNx lie between those of the Pd foil and PdO references (Fig. 2e), indicating an oxidation state of Pd between 0 and + 2. Fourier transformed extended X-ray absorption fine structure (EXAFS) spectra exhibit a dominant feature at 1.50 Å, revealing the presence of Pd–N coordination in Pd SA/BCNx (Fig. 2f)[48,49]. No Pd–Pd coordination peaks are detected at 2.96 Å and 2.45 Å, confirming that the Pd species in Pd SA/BCNx are atomically dispersed without metallic Pd or PdO clusters. The EXAFS fitting results suggest that the Pd single-atom site in Pd SA/BCNx is close to a Pd–N_3 coordination site (Fig. 2g, Supplementary Fig. 3 and Supplementary Table 2). The Pd–N coordination is also visually reflected from wavelet transform (WT) EXAFS analysis of Pd SA/BCNx (Fig. 2h–j), showing a single intensity maximum only in the lobes centered at 6.30 $Å^{-1}$ in *k*-space, corresponding to the N atoms around Pd. The molecular structure model of Pd SA/BCNx is determined from the XPS and solid-state ^{11}B NMR results (inset of Fig. 2g).

Photocatalytic C–N coupling for glycine production

Photocatalytic C–N coupling reaction for the glycine production was attempted in an aqueous solution of EG and NO_3^- (Fig. 3a). The reaction comprises two fundamental steps of EG photooxidation and NO_3^- photoreduction. The EG solution (0.1 M) in the reaction was prepared via hydrolysis of PET plastic (Methods, Supplementary Fig. 4). First, the ^{1}H NMR spectra of commercial GA, EG and glycine were applied to determine the characteristic peaks of the substrate (EG, 3.52 ppm), the target product (glycine, 3.40 ppm), and the byproduct (GA, 4.10 ppm) (Supplementary Fig. 5). Some metal oxides, metal sulfides, and carbon nitride (g-C_3N_4), have been demonstrated to effectively catalyze the conversion of EG into aldehyde-containing intermediates, thereby meeting the necessary conditions for photocatalytic C–N coupling[10,11,14,32]. Subsequently, a series of photocatalysts was screened, including metallic oxides (ZnO, TiO_2, WO_3), metallic sulfides (CdS, MoS_2) and g-C_3N_4 (B-free carbon nitride, CN; B atom-doped carbon nitride, BCNx), for glycine photosynthesis from EG and NO_3^- (Fig. 3b and Supplementary Fig. 6a). Metal oxide catalysts inevitably lead to the formation of formic acid (FA), whereas metal sulfide- and g-C_3N_4-based catalysts do not exhibit this phenomenon, primarily due to the over-oxidation of EG occurring on metal oxides. Based on these preliminary screening results, the BCNx demonstrates the optimal catalytic performance, achieving a glycine selectivity close to 100% and a reaction activity of 0.82 mmol g_{cat}^{-1} h^{-1}. The introduction of metal single-atoms onto BCNx support can generate strong electronic interactions, which

https://doi.org/10.1038/s41467-026-68666-z

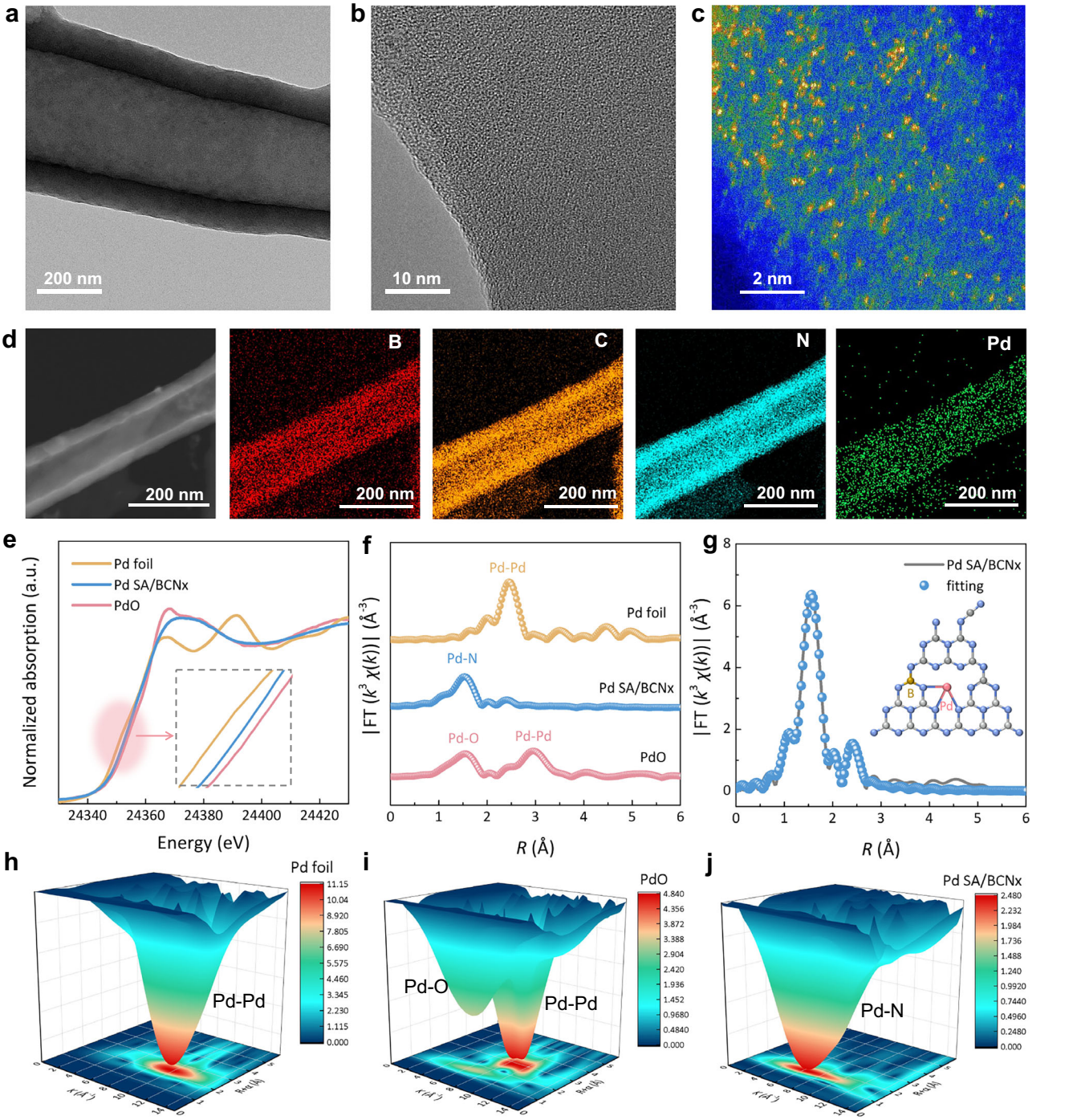

Fig. 2 | Structural characterization of the Pd SA/BCNx catalyst. a TEM image, (**b**) HR-TEM image, (**c**) aberration-corrected HAADF-STEM image, (**d**) HAADF-STEM image and EDS elemental mapping images of C, N, B, and Pd elements in Pd SA/BCNx. **e** Normalized XANES spectra and (**f**) k^3-weighted Fourier transform Pd *K*-edge EXAFS spectra of Pd foil, Pd SA/BCNx and PdO. Inset: the enlarged image of the absorption edge for three samples. **g** Pd *K*-edge EXAFS (line) and curve fitting (points) for Pd SA/BCNx, shown in k^3-weighted R-space. The inset depicts the structure of Pd SA/BCNx. The blue sphere represents the N element, the gray sphere represents the C element, the brown sphere represents the B element, and the pink sphere represents the Pd element. Wavelet-transformed k^3-weighted EXAFS spectra of (**h**) Pd foil, (**i**) PdO and (**j**) Pd SA/BCNx.

are expected to optimize the light absorption, charge transfer and separation capabilities[39], as well as enhance the catalytic activity for C −N coupling reactions. Specifically, different metal single-atoms (Pt, Pd, Au, Ag, Cu, Co and Fe) were anchored on the BCNx support to construct dual active site catalysts to increase glycine production activity (Fig. 3c and Supplementary Fig. 6b). The catalytic performance reveals that the Cu SA/BCNx cannot significantly improve the catalytic activity, and the Pt/Fe SA/BCNx reduce the selectivity towards glycine due to the formation of more AA by-products. In contrast, Pd/Au/Ag/Co SA/BCNx catalysts achieve increased rates of glycine generation and maintain high selectivity with a small amount of GA product. Notably, the Pd SA/BCNx achieves the highest glycine generation rate of 2.9 mmol g_{cat}^{-1} h^{-1} with a selectivity of 92%, and this performance is competitive (Supplementary Table 3). Moreover, the apparent

https://doi.org/10.1038/s41467-026-68666-z

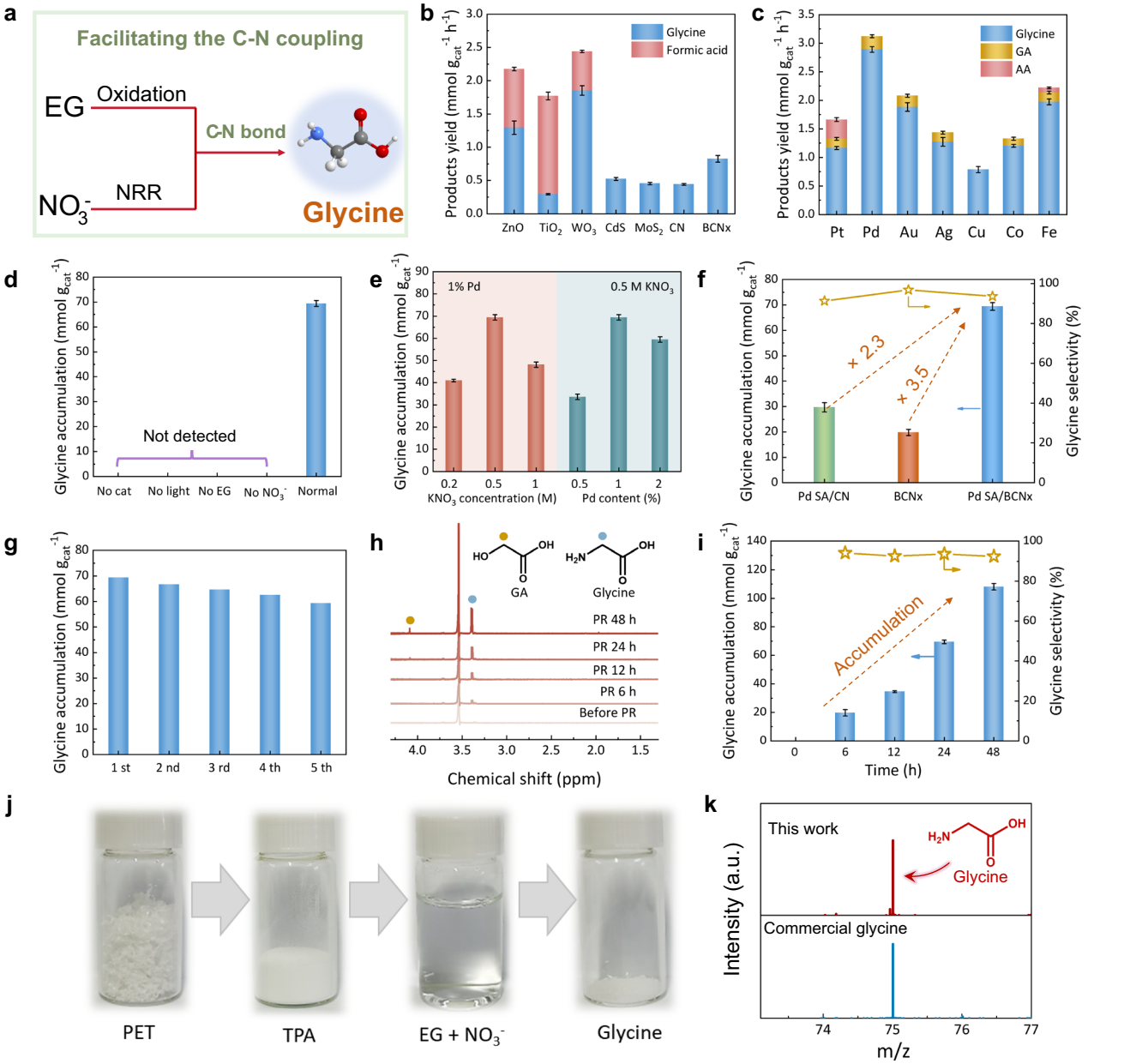

Fig. 3 | Photocatalytic C–N coupling for glycine production. a Schematic illustration of the photocatalytic synthesis of glycine from EG and nitrate. The blue sphere represents the N element, the gray sphere represents the C element, the red sphere represents the O element, and the white sphere represents the H element. The arrow represents conversion or formation. **b** Glycine production rates over various types of semiconductors. **c** Glycine production rates over various metal single-atom anchored BCNx catalysts, including Pt, Pd, Au, Ag, Cu, Co and Fe. Reaction conditions: 20 mg photocatalyst, 50 mL 0.1 M EG/0.5 M NO_3^- solution, T = 25 °C, Ar atmosphere, t = 24 h, and 300 W Xe lamp (320 nm < λ < 780 nm). **d** The yield of glycine within 24 h under various reaction conditions. Not detected represents the product could not be detected due to exceeding the detection limit of the instrument. **e** Control experiments of BCNx with different Pd loadings in 0.5 M KNO_3 and different concentrations of KNO_3 over Pd SA/BCNx (1 wt% Pd). **f** The yield of glycine within 24 h over Pd SA/CN, BCNx and Pd SA/BCNx. The left Y-axis represents glycine accumulation, and the right Y-axis represents selectivity. These dashed arrows represent multiples of growth. **g** Evaluation of recycling stability. **h** ^{1}H NMR spectra during the photocatalytic reaction. **i** Long-term accumulation profiles for glycine produced over Pd SA/BCNx. The dashed arrow represents glycine accumulation. **j** Schematic diagram of EG photoconversion to glycine in PET hydrolysate over Pd SA/BCNx. **k** Glycine products derived from the reaction through gas chromatography–mass spectrometry (GC–MS) analyses. The arrow represents the direction towards glycine. Error bars represent the standard deviations from the means of at least three repeated experiments.

quantum efficiency (AQE) can reach 0.39% under monochromatic irradiation at 365 nm (Supplementary Fig. 7).

A series of control experiments were conducted to further investigate the catalytic mechanism and identify key factors influencing the reaction. No glycine was detected under conditions lacking light, catalyst, EG or NO_3^- (Fig. 3d), indicating that the reaction is a photocatalytic C–N coupling process driven by EG and NO_3^- in the presence of the Pd SA/BCNx catalyst. The reaction conditions were further optimized as 1% Pd loading on BCNx and 0.1 M EG/0.5 M KNO_3 (Fig. 3e), indicating that the Pd and NO_3^- concentrations play crucial roles in the catalytic activity. Furthermore, when a mixture of anhydrous EG and KNO_3 was subjected to photocatalytic C–N coupling, no glycine product was observed (Supplementary Fig. 8), revealing that water is indispensable in this system. Subsequently, the synergistic effect of Pd and B sites in photocatalytic C–N coupling for glycine production was investigated. All three catalysts (Pd SA/CN, BCNx, Pd

SA/BCNx) exhibit glycine selectivity exceeding 92% (Fig. 3f), suggesting that the high selectivity does not primarily rely on the modulation of electronic structure and optical properties of the support by Pd doping or B sites. Compared to metal oxides, the g-C_3N_4-based support plays a key role in achieving highly selective photosynthesis of glycine (Fig. 3b). The Pd SA/BCNx demonstrates the highest glycine production activity of 69.4 mmol g_{cat}^{-1}, approximately 3.5 times that of the BCNx (19.6 mmol g_{cat}^{-1}) and 2.3 times that of the B-free Pd SA/CN catalyst (29.7 mmol g_{cat}^{-1}) (Fig. 3f), indicating that stronger interactions between the Pd–B diatomic sites can synergistically enhance the catalytic activity. The conversion efficiency of EG and NO_3^- on the Pd SA/BCNx catalyst are 23.4% and 5.6%, respectively, within 24 h (Supplementary Fig. 9), and the total molar amount of detected products (glycine and GA) was approximately equal to the amount of consumed EG. In addition, the glycine production activity of the Pd nanoparticle-loaded catalysts (Pd NP/BCNx, 40.9 mmol g_{cat}^{-1}) was comparatively lower than that of the Pd SA/BCNx (Supplementary Fig. 10), which may be attributed to the fact that atomic Pd can expose more active sites, thereby enhancing the selective adsorption and activation of key intermediates to facilitate the C–N coupling process.

In addition to catalytic activity, long-term stability is also a crucial factor for practical applications. The Pd SA/BCNx catalyst exhibits recycling stability, with no significant decrease in glycine production observed after five cycles (Fig. 3g). The XRD, FT-IR, and TEM images reveal that the crystal structure, chemical composition, and microstructure of the Pd SA/BCNx remain unchanged after the reaction (Supplementary Fig. 11). Quantitative analysis of the ^{1}H NMR spectra (Fig. 3h) reveals that the yield of glycine increased linearly with increasing time while maintaining high selectivity (> 92%) (Fig. 3i). Notably, the selective production of glycine alone is achieved by precisely controlling the reaction time within 24 h, which significantly simplifies the subsequent separation and purification steps for the target product (Fig. 3j). The target product was isolated and characterized using gas chromatography–mass spectrometry (GC–MS). The characteristic peak observed at m/z = 75 in the mass spectrum matched that of the commercial glycine standard (Fig. 3k), indicating the promising application of the dual-site Pd–B catalyst for efficient glycine photosynthesis.

Photocatalytic mechanism

A series of photoelectric characterizations were performed to elucidate the underlying mechanism of the photocatalytic glycine generation. Initially, the light absorption capabilities of the samples were evaluated via UV–vis diffuse reflectance spectroscopy. Compared with pure CN, both BCNx and Pd SA/BCNx exhibit significantly improved UV–visible light absorption (Fig. 4a), which can be attributed to the local electron reconstruction induced by the incorporation of Pd–B diatomic sites and C ≡ N groups[50]. Based on Tauc plot analysis, the bandgap energies are calculated to be 2.45 eV (CN) and 2.20 eV (BCNx, Pd SA/BCNx) (Supplementary Fig. 12a). The XPS valence band spectra reveal valence band maximum positions of CN, BCNx and Pd SA/BCNx at 1.62 eV, 1.52 eV and 1.46 eV, respectively (Supplementary Fig. 12b). The result indicate that the band structure (Supplementary Fig. 12c) fulfils the redox potential of EG oxidation to glycolaldehyde (0.55 eV)[32] and NO_3^- reduction to NH_4^+/NH_3 (−0.58 eV)[51,52].

The separation efficiency of photoinduced carriers was investigated through integrated photoluminescence (PL) and time-resolved PL (TR-PL) measurements. The PL spectra reveal that the emission intensity of Pd SA/BCNx is significantly quenched (Supplementary Fig. 13a), which can be attributed to the rapid electron transfer from the B atom site to the Pd atom site. Moreover, the TR–PL spectra show that the average emission lifetime of Pd SA/BCNx (τ_{ave} = 2.15 ns) is markedly shorter than that of BCNx (τ_{ave} = 2.36 ns) and CN (τ_{ave} = 15.49 ns) (Supplementary Fig. 13b and Supplementary Table 4), confirming that the strong electronic interactions between the Pd–B diatomic sites effectively suppress the recombination of charge carriers. The charge separation behavior of Pd SA/BCNx was also further confirmed through transient photocurrent response (TPR) and electrochemical impedance spectroscopy (EIS) measurements. Compared with BCNx and CN, the Pd SA/BCNx exhibits a greater photocurrent response (Supplementary Fig. 13c) and a smaller semicircle diameter in the EIS Nyquist plots (Supplementary Fig. 13d), indicating its enhanced efficiency in electron-hole pair separation and transfer.

In situ XPS was conducted under dark and illuminated conditions to explore the enhanced electronic interaction and photoelectron transfer dynamics between the atomic Pd site and the B site in Pd SA/BCNx during the photocatalytic process. Under illumination, the binding energy peak of the B–N bond shifts to a higher binding energy by 0.2 eV, whereas the peaks of $Pd^{\delta+}$ shift to a lower binding energy by 0.2 eV (Fig. 4b, c). Both peaks revert to their original positions upon cessation of illumination, indicating that electrons can rapidly transfer from the B site to the atomic Pd site upon illumination. This dynamic electronic modulation is crucial for optimizing the redox reaction sites during glycine synthesis pathways. Furthermore, density functional theory (DFT) calculations reveal that the introduction of B confirms the strong electron interactions between the atomic Pd site and the B site (Supplementary Fig. 14). Femtosecond transient absorption spectroscopy (fs-TAS) was employed to investigate the photoelectron transfer kinetics of Pd SA/BCNx and BCNx (Fig. 4d–g). Upon excitation with a 400 nm pump pulse, both Pd SA/BCNx and BCNx are excited from the ground state to the excited state, with the probe wavelength ranging from 410 nm to 750 nm. The TAS of BCNx exhibits a distinct negative peak at ~ 440 nm (Fig. 4e, g), corresponding to ground-state bleaching, indicating the relaxation process of the excited state. In contrast, the signal intensity at 440 nm for Pd SA/BCNx is significantly weaker than that of BCNx, and an additional negative peak at ~ 560 nm is observed at early delay times (Fig. 4d, f). The kinetic analysis of the absorption decay curve reveals the average ground-state bleaching (GSB) recovery times of BCNx (314.88 ps) and Pd SA/BCNx (264.12 ps), respectively (Fig. 4h and Supplementary Table 5), suggesting efficient the photoelectron transfer from the BCNx to the Pd atom (Fig. 4i)[53]. These results highlight the pivotal role of the Pd–B diatomic sites in enhancing light absorption, optimizing band structure, and accelerating the photoelectron transfer dynamics.

An in-depth mechanistic study was conducted to explore the reaction mechanisms of photocatalytic C–N coupling for glycine production. First, the role of photogenerated electron–hole pairs in glycine photosynthesis was investigated by introducing different scavengers (Fig. 5a). The addition of 0.1 M nitrobenzene as an electron scavenger significantly reduces the glycine yield from 69.4 to 11.6 mmol g_{cat}^{-1}, indicating that photogenerated electrons are crucial for NO_3^- reduction. Moreover, the introduction of 0.1 M phenol as a hole scavenger into the reaction leads to a decrease in the glycine production to 3.9 mmol g_{cat}^{-1}, revealing that photogenerated holes predominantly drive the oxidation of EG. Moreover, when 0.1 M 5,5-dimethyl-1-pyrroline N-oxide (DMPO, a sacrificial radical agent) was added, the glycine yield also decreases substantially to 19.8 mmol g_{cat}^{-1}, suggesting that the formation of glycine may also be driven by photogenerated radicals.

Furthermore, in situ electron spin resonance spectroscopy (ESR) was performed using a hole-trapping agent (2,2,6,6-tetramethylpiperidine-1-oxyl, TEMPO) and the radical trapping agent DMPO. Under light irradiation, the signal peak of TEMPO-h^+ significantly weakens in pure H_2O (Supplementary Fig. 15), suggesting that light can induce the generation of numerous photogenerated holes in Pd SA/BCNx that participate in oxidation reactions. Quantitative ESR analysis was conducted for Pd SA/CN and Pd SA/BCNx under the same TEMPO concentration (Fig. 5b). The TEMPO signal peaks are the lowest in the Pd SA/BCNx system under illumination, demonstrating that the incorporation of B-atom sites promotes the rapid

https://doi.org/10.1038/s41467-026-68666-z

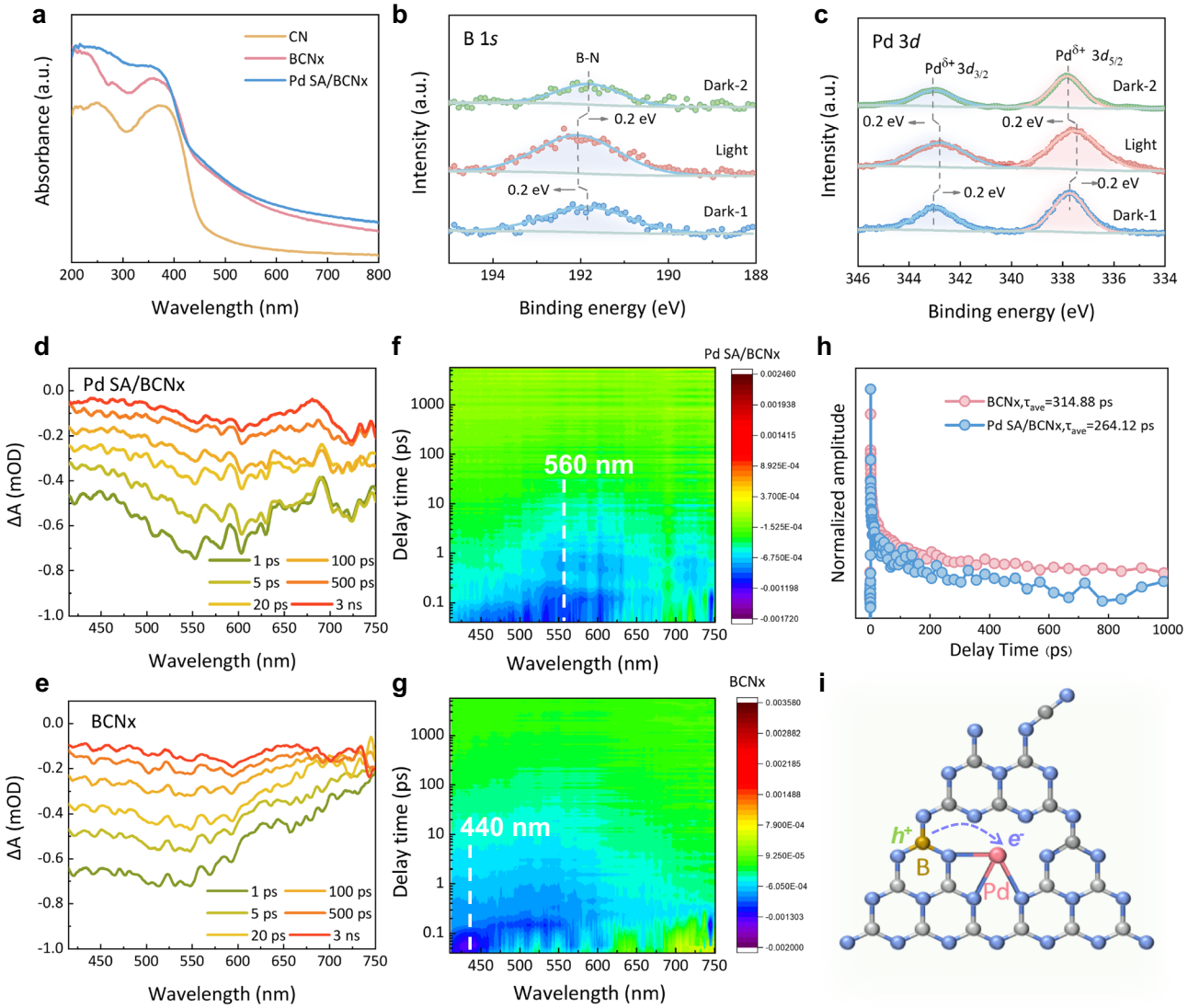

Fig. 4 | Optoelectronic characterization and photoelectron transfer dynamics study. a UV–vis diffuse reflectance spectra of CN, BCNx and Pd SA/BCNx. In situ XPS spectra of (**b**) B 1*s* and (**c**) Pd 3*d* of Pd SA/BCNx before and after light illumination. These shadings represent B-N bonding or different Pd elemental orbitals. These arrows represent the direction of peak shift. TAS signals of (**d**) Pd SA/BCNx and (**e**) BCNx on the ps-ns timescale. 2D mapping fs-TAS of (**f**) Pd SA/BCNx and (**g**) BCNx. **h** Normalized TA kinetic curves of BCNx and Pd SA/BCNx. **i** Photoelectron transfer pathway between the atomic Pd site and the B site in Pd SA/BCNx. The blue sphere represents the N element, the gray sphere represents the C element, the brown sphere represents the B element, and the pink sphere represents the Pd element. The dashed arrows in i represents the direction of electron transfer.

accumulation of photogenerated holes. When H_2O oxidation matches the oxidation reaction, the signals of DMPO-OH are recorded, corresponding to hydroxyl radicals (•OH) produced by the oxidation of water by photogenerated holes (Fig. 5c). Notably, upon introducing EG into the reaction system, a typical sextet signal characteristic of an alkoxy radical (•$CHOHCH_2OH$, $A_N = 15.9$ G, $A_H = 22.7$ G) appeared in the ESR spectrum (Fig. 5d and Supplementary Fig. 16)[10,54]. However, the signal peak of DMPO-OH completely disappears, indicating that the oxidation of EG takes precedence over H_2O oxidation by photogenerated holes to produce •$CHOHCH_2OH$. When both EG and NO_3^- are present simultaneously, the •$CHOHCH_2OH$ signal peak further intensifies, suggesting that NO_3^- is preferentially reduced over water to consume more photogenerated electrons, further demonstrating that the generation of •$CHOHCH_2OH$ is directly related to the increase in glycine yield. In addition, no •O_2^- or H_2O_2 is produced in the pure H_2O, EG and EG/NO_3^- systems, indicating that the oxidation reaction is only driven by the photogenerated holes (Supplementary Fig. 17). Subsequently, comparing the gas-phase products in the three systems (Supplementary Fig. 18), it is found in the pure H_2O system, Pd SA/BCNx is more inclined to undergo photocatalytic overall H_2O splitting, producing trace amounts of H_2 and O_2. In the EG aqueous solution system, the EG molecules more readily consume the holes, causing Pd SA/BCNx to generate more photogenerated electrons for reducing H_2O to H_2. However, in the EG/ NO_3^- system, no gaseous products are detected, suggesting that the photogenerated electrons are exclusively utilized for the reduction of NO_3^-. The above results indicate that EG molecules can be effectively activated to form •$CHOHCH_2OH$ through dehydrogenation, thereby generating an H-C=O precursor for the subsequent C–N coupling[40]. Therefore, photogenerated holes predominantly drive the oxidation of EG to generate alkyl radicals, whereas photogenerated electrons mainly participate in the reduction of NO_3^- to form nitrogen intermediates (NO_2^-, NH_3, or NH_4^+). The generation of alkyl radicals and nitrogen intermediates creates favorable conditions for the subsequent C–N coupling reaction.

https://doi.org/10.1038/s41467-026-68666-z

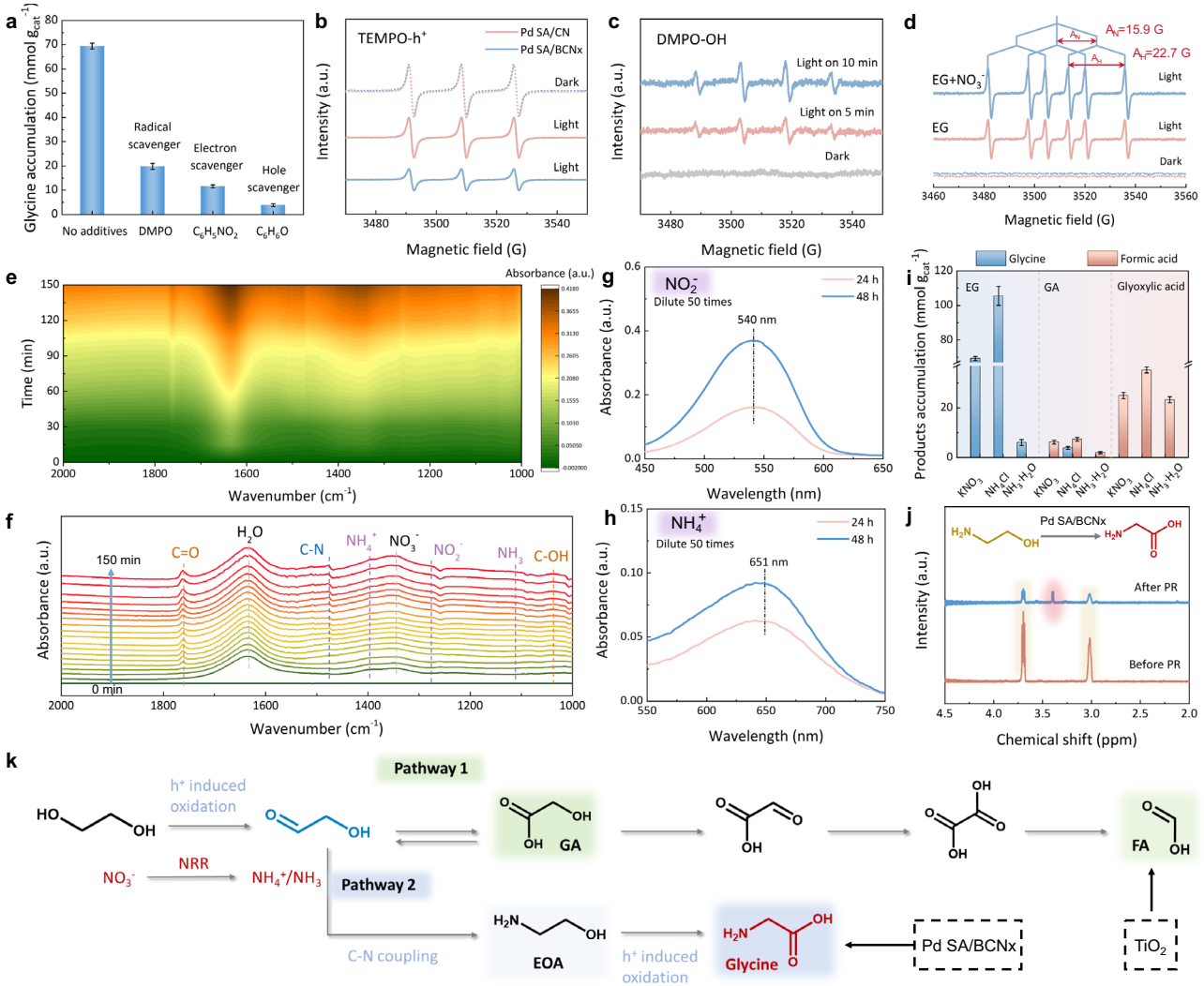

Fig. 5 | Identification of key intermediates and reaction pathways for photocatalytic C–N coupling in glycine production. a Control experiments utilizing different scavengers under reaction conditions with 20 mg of photocatalyst, 50 mL of 0.1 M EG/0.5 M NO_3^- solution, 0.1 M scavenger, T = 25 °C, an Ar atmosphere, t = 24 h, and a 300 W Xe lamp (320 nm < λ < 780 nm). **b** Quantitative ESR spectra of photoinduced holes before and after a duration of 10 min under illumination using TEMPO on Pd SA/CN and Pd SA/BCNx. **c** ESR spectra of hydroxyl radicals generated using DMPO over Pd SA/BCNx in pure H_2O. **d** In situ quantitative ESR spectra for Pd SA/BCNx in EG and EG/NO_3^- solutions in the presence of DMPO. **e**, **f** In situ ATR −FTIR spectra of the photocatalytic C–N coupling reaction over Pd SA/BCNx. UV–vis spectra of (**g**) NO_2^- and (**h**) NH_4^+ in the photocatalytic reaction solution at 24 h and 48 h over Pd SA/BCNx. **i** Control experiments with various reactants over Pd SA/BCNx under reaction conditions with 20 mg of photocatalyst, 50 mL of 0.1 M reactants (ethylene glycol, glycolic acid, glyoxylic acid)/0.5 M NO_3^-, NH_4Cl or $NH_3 \cdot H_2O$ solution, T = 25 °C, an Ar atmosphere, t = 24 h, and a 300 W Xe lamp (320 nm < λ < 780 nm). **j** ^{1}H NMR spectra before and after photocatalytic conversion involving 0.02 M ethanolamine over Pd SA/BCNx. Yellow represents ethanolamine, and pink represents the glycine product. **k** Proposed mechanism and reaction pathway for glycine production from the photocatalytic conversion of EG and NO_3^-. Error bars represent the standard deviation of the mean from at least three independent replicate experiments. These arrows represent conversion or formation.

After identifying the key factors driving the enhanced efficiency of glycine synthesis by the Pd SA/BCNx catalyst, in situ attenuated total reflection Fourier transform infrared spectroscopy (ATR−FTIR) was employed to investigate the key intermediates in the glycine photosynthesis. The in situ ATR−FTIR spectra clearly reveal information on intermediates formed in two pathways of EG oxidation (yellow label) and NO_3^- reduction (purple label) (Fig. 5e, f). For the NO_3^- reduction pathway, characteristic stretching vibration bands of NO_2^- (1280 cm^{-1}), NH_3 (1120 cm^{-1}) and NH_4^+ (1400 cm^{-1}) are detected[12,55,56], and their intensities increase progressively with reaction time. Furthermore, UV −vis spectroscopy analysis confirms the presence of absorption peaks at 540 nm and 651 nm, corresponding to the characteristic absorptions of complexes formed by NO_2^- and NH_4^+ ions, respectively (Fig. 5g, h)[21]. Thus, NH_4^+ and NH_3 are identified as the main products of nitrate reduction, and NO_2^- is regarded as the primary intermediate. For the EG oxidation pathway, a characteristic C=O stretching vibration peak of the key intermediate glycolaldehyde was observed at 1760 cm^{-1}. The C−OH vibrational band at 1030 cm^{-1} could be attributed to glycolaldehyde, ethanolamine (EOA) or glycine[57]. Notably, a distinct C−N vibrational band at 1479 cm^{-1} belongs to glycine or EOA[5], and its intensity increased steadily throughout the reaction. Therefore, glycolaldehyde, EOA and NH_4^+/NH_3 are likely to be the critical intermediates for the C−N coupling reaction in glycine photosynthesis.

A series of designed control experiments were conducted to further identify the critical intermediates involved in the C−N coupling reaction. When EG and different ammonium salts (NH_4Cl, $(NH_4)_2SO_4$ and $(NH_4)_2CO_3$) were used as reactants, the glycine yield was significantly increased to 105.5 mmol g_{cat}^{-1}, 80.8 mmol g_{cat}^{-1} and

90.6 mmol g_{cat}^{-1}, respectively, compared with that of the EG/KNO_3 system (69.4 mmol g_{cat}^{-1}) (Fig. 5i and Supplementary Figs. 19, 20). In addition, trace amounts of glycine (6.0 mmol g_{cat}^{-1}) can still be found in the EG/NH_3•H_2O system. In contrast, the glycine yield is undetectable in the EG/NH_2OH system, indicating that NH_4^+ and NH_3 are the key intermediates for the C–N coupling process during the photoreduction half-reaction (NO_3^- to NH_4^+/NH_3). Moreover, in the conventional oxidation pathway of EG (Fig. 5k, Pathway 1)[32], glycolaldehyde is generated via the oxidative dehydrogenation of EG and can be further oxidized to FA byproducts.

A series of control experiments were also performed to identify the key intermediates at the oxidation end. When GA is used as a substrate to react with NO_3^-, NH_4^+, NH_3 and NH_2OH, only trace amounts of glycine can be detected in the GA/NH_4^+ system, whereas the formation of FA can be observed in the NO_3^-, NH_4^+ and NH_3 systems. When glyoxalic acid was used as the substrate instead of GA, the FA yields in all three systems further increased without any production of glycine. Therefore, glycolaldehyde from the oxidation and dehydrogenation of EG serves as the key intermediate for the C–N coupling process in the photooxidation half-reaction (EG to glycolaldehyde). Similar results were also observed with the pure CN catalyst, although the glycine yield was lower than that of Pd SA/BCNx (Supplementary Fig. 21), suggesting that the g-C_3N_4-based support follows the same reaction pathway, and the introduction of Pd–B diatomic sites significantly enhances the C–N coupling reaction.

After identifying the key intermediates, the subsequent reaction pathways were explored. It was hypothesized that glycolaldehyde would then undergo a preliminary C–N coupling reaction between the aldehyde groups and NH_4^+/NH_3 to generate the EOA intermediate. Subsequently, EOA is proposed to be further oxidized to glycine. To validate this hypothesis, the Pd SA/BCNx was subjected to a photocatalytic reaction in a 0.02 M EOA solution. The ^{1}H NMR spectra reveal a decrease in the characteristic peaks of EOA over time, accompanied by the appearance of peaks corresponding to glycine (Fig. 5j), thereby confirming the oxidation of EOA to glycine catalyzed by the Pd SA/BCNx, consistent with the reported results[58,59]. A comparison of glycine yields for EOA oxidation was performed over CN, BCNx, Pd SA/CN and Pd SA/BCNx, and the results reveal that the glycine yields are significantly higher for B-containing catalysts than B-free catalysts, with the yield achieved by BCNx even surpassing that of Pd SA/CN. This observation further substantiated that the oxidation of EOA primarily occurs at the hole-rich B site (Supplementary Fig. 22). Therefore, it was inferred that the key intermediate glycolaldehyde may undergo two pathways during the reaction. The pathway 1 involves further oxidation of glycolaldehyde to form GA, and the pathway 2 involves the amination of glycolaldehyde to form EOA (Fig. 5k and Supplementary Fig. 23a). The high glycine selectivity exhibited by the Pd SA/BCNx may be attributed to its enhanced capability to facilitate the amination of glycolaldehyde, facilitating the timely formation of EOA (Fig. 3b, c). In addition to the spectroscopic evidence mentioned above, DFT calculations were employed to investigate the reaction energies for two pathways over TiO_2 and Pd SA/BCNx. The conversion of glycolaldehyde to GA was found to possess a larger negative reaction energy on TiO_2 than Pd SA/BCNx, indicating that TiO_2 is more favorable for the oxidation of EG to GA (Pathway 1), which is further oxidized to produce FA by-products (Supplementary Fig. 23b). In contrast, the Pd SA/BCNx surface is more inclined to promote the amination of glycolaldehyde to form EOA (Supplementary Fig. 23c), which is further oxidized to glycine (Pathway 2). These results provide a rational theoretical explanation for the high selectivity of Pd SA/BCNx for glycine production. However, due to the inherent simplification of DFT, there are still limitations in accurately capturing the real catalytic process when simulating catalytic conditions.

Based on the aforementioned experimental results, a possible reaction mechanism is proposed to elucidate the photosynthesis of glycine from EG and NO_3^- (Fig. 5k, Pathway 2). First, under illumination, electrons in the valence band of the Pd SA/BCNx catalyst are excited to the conduction band, resulting in photogenerated electron and hole pairs. The photogenerated holes oxidize EG to glycolaldehyde via a dehydrogenation process. The photogenerated electrons facilitate the reduction of NO_3^- to NH_4^+/NH_3. The basic nitrogen in NH_4^+/NH_3 contains attacks the electrophilic aldehyde group carbon of glycolaldehyde, initiating a C–N coupling reaction to form EOA[60]. The generated EOA is further oxidized to glycine by photogenerated holes[58,59]. During the photocatalytic process, the introduction of Pd–B diatomic sites, along with strong interaction between Pd and B atoms, significantly enhances the light absorption and accelerates electron transfer from B site to Pd site, thereby synergistically enhancing the redox capacity and facilitating the photocatalytic C–N coupling reaction towards glycine formation. More importantly, compared with conventional metal oxide photocatalysts, the Pd–B diatomic sites stabilize and drive the glycolaldehyde intermediate to complete the C–N coupling pathway while effectively suppressing its over-oxidation into byproducts, resulting in high selectivity for glycine production.

Photocatalytic conversion of gram-scale real-world PET plastic and nitrate to glycine

The photocatalytic conversion of gram-scale real-world PET plastic and nitrate to glycine was performed to validate the practical applicability. Glycine yields were achieved with 101.3 mmol g_{cat}^{-1} (PET powder), 71.1 mmol g_{cat}^{-1} (PET clothes), 89.4 mmol g_{cat}^{-1} (PET bottle), 73.0 mmol g_{cat}^{-1} (PET bag), 68.9 mmol g_{cat}^{-1} (PET box) and 43.7 mmol g_{cat}^{-1} (PET towel) using 10 g of real-world PET plastics as feedstock (Fig. 6a). Furthermore, this photocatalytic strategy demonstrates versatility, enabling its application to biomass-derived methanol and glycerol for photocatalytic C–N coupling reactions (Fig. 6b). When methanol and NO_3^- are used as reactants, the system selectively produced formamide. Conversely, when glycerol reacted with NO_3^-, glycine was successfully synthesized, possibly because glycerol can involve both the C–C bond cleavage step and the C–N coupling reaction. This finding further confirms the broad substrate applicability of this catalytic system, ranging from plastics to biomass. Furthermore, considering practical application scenarios, the impact of other ions commonly present in real environments on the reaction was evaluated. The introduction of ionic salts (Na^+, Ca^{2+}, Cl^-, SO_4^{2-}, HPO_4^{2-}, etc.) and wastewater exerted varying degrees of inhibitory effects on glycine production. Despite this inhibition, the glycine yield remained above 33.2 mmol g_{cat}^{-1} in real-world wastewater (Fig. 6c), preliminarily demonstrating the potential practical application of this system. Nevertheless, the composition of real wastewater is often highly complex and variable, and the application of the system necessitates further in-depth and systematic investigation. Future research efforts should focus on enhancing the resistance of the catalysts to interference and further optimizing reaction conditions to significantly improve the glycine yield.

A solar-driven photocatalytic glycine synthesis experiment was conducted by using a 30×30 cm^2 plastic Fresnel lens as an economical and efficient solar concentrator (Fig. 6d). The results demonstrated that after 6 h of daily sunlight exposure, the glycine yield consistently remained between 10 and 20 mmol g_{cat}^{-1} under different weather conditions, with selectivity maintained at 100% (Fig. 6e and Supplementary Fig. 24). Upon scaling up the reaction volume to 500 mL (Supplementary Fig. 25), the glycine yields further increased to 32.3 mmol g_{cat}^{-1}. These findings confirm the feasibility of efficiently producing glycine using actual solar energy, laying a solid foundation for practical applications. Furthermore, the environmental impact of this catalytic system was also evaluated (Supplementary Fig. 26). Compared to conventional landfilling or incineration, processing 50,000 tons of waste plastic annually could prevent the emission of ~104 kt of CO_2. Moreover, effective treatment of NO_3^- in industrial

https://doi.org/10.1038/s41467-026-68666-z

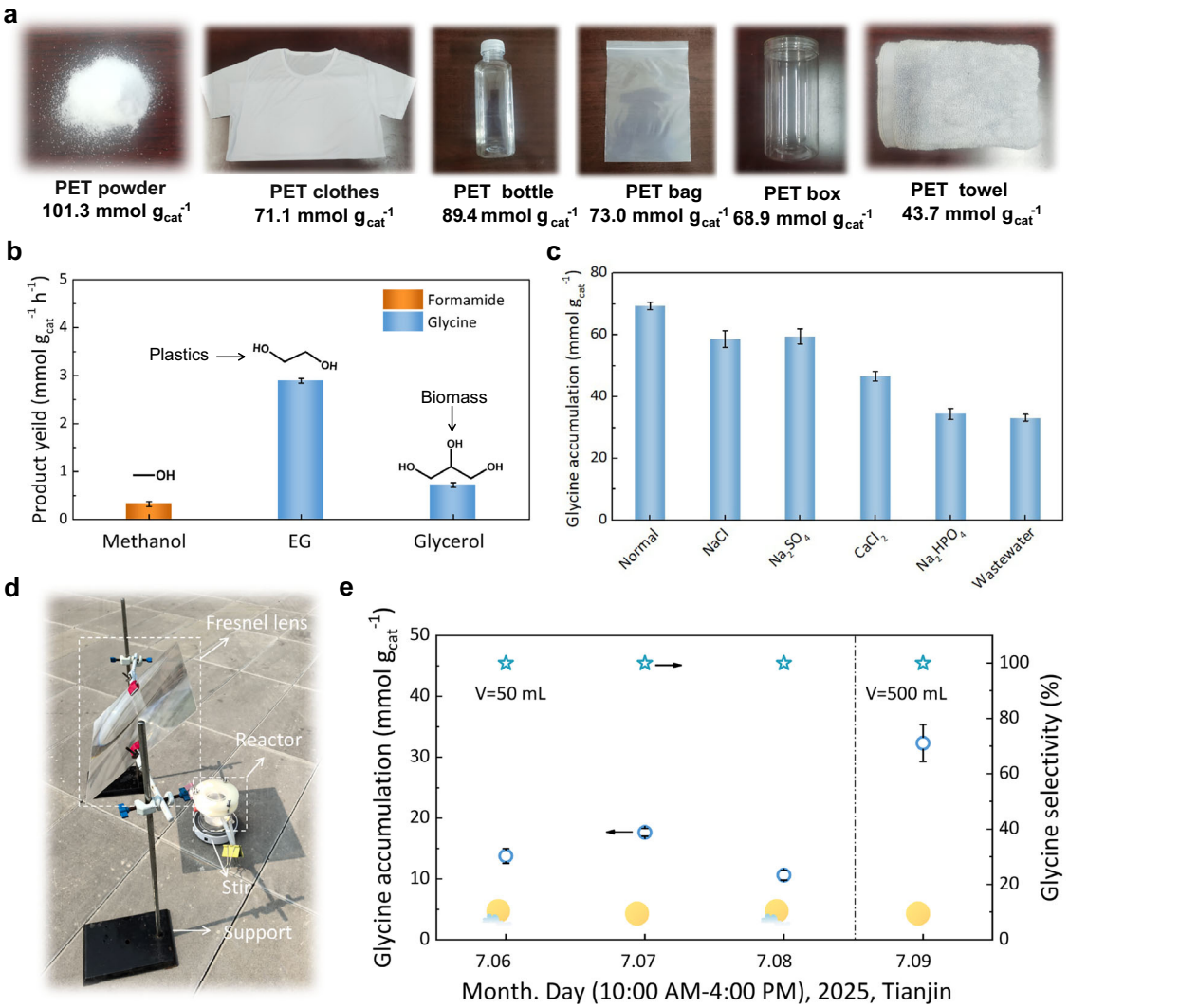

Fig. 6 | Photocatalytic C–N coupling of real-world post-consumer PET plastics and nitrate at the gram-scale (10 g). a Photographs of real-world post-consumer PET plastics samples and the corresponding glycine yields obtained within 24 h. **b** Glycine yield produced through photocatalytic C–N coupling reactions between methanol, EG and glycerol. **c** Comparison of glycine yield over Pd SA/BCNx in the presence of various ionic salts (0.5 M) or real-world wastewater, including Na^+ (~48.48 mM), Ca^{2+} (~5 mM), K^+ (~10.2 mM), Cl^- (~14.08 mM), SO_4^{2-} (~5.21 mM), NO_3^- (~8.2 mM) and HPO_4^{2-} (~2.11 mM). **d** Schematic diagram of the experimental setup for photocatalytic glycine production utilizing real sunlight. **e** Corresponding glycine yield and selectivity under different weather conditions and container sizes. Error bars represent the standard deviation of the mean from at least three independent replicate experiments.

wastewater could prevent the release of ~147 kt of NO_3^- into groundwater or oceans annually. Consequently, this photocatalytic system not only holds significant potential for substantial commercial value but also demonstrates the possibility of achieving zero emissions for both CO_2 and NO_3^-, contributing significantly to environmental sustainability.

Discussion

This work presents an attractive "waste-to-wealth" strategy for the photosynthesis of glycine via C–N coupling between waste PET-derived EG and NO_3^-, utilizing a Pd–B diatomic site catalyst. The optimized Pd–B diatomic catalyst exhibits a glycine generation rate of 2.9 mmol g_{cat}^{-1} h^{-1} with selectivity exceeding 92%. During the photocatalysis, EG is selectively photo-oxidized to glycolaldehyde, while NO_3^- is photo-reduced to NH_4^+/NH_3. Subsequently, glycolaldehyde and NH_4^+/NH_3 engage in C–N coupling to generate glycine. The Pd–B diatomic site demonstrates advantages in stabilizing and facilitating the progression of glycolaldehyde along the C–N coupling pathway, and suppressing its over-oxidation into organic acids, thereby achieving high selectivity for glycine. This process can be extended to the transformation of g-scale real-world PET plastic and biomass-derived polyols into glycine under real sunlight. Future research will focus on the design and optimization of reactors, aiming to fully unlock the substantial potential of this "win-win" system for large-scale applications.

Methods

Materials

Titanium dioxide (anatase TiO_2, particle size < 25 nm), zinc oxide (ZnO, particle size < 50 nm), tungsten trioxide (WO_3, particle size < 50 nm), molybdenum disulfide (MoS_2) and cadmium sulfide (CdS) were purchased from Shanghai Aladdin Biochemical Technology Co., Ltd., and characterized (Supplementary Fig. 27). Melamine, sodium hydroxide (NaOH), sodium cyanoborohydride ($NaBH_3$-CN), glyoxylic acid, ethanolamine and glycine were obtained from Shanghai Aladdin Biochemical Technology Co., Ltd. Palladium(II) chloride ($PdCl_2$), ethylene glycol (EG), glycolic acid (GA), methanol, glycerol, nitrobenzene, phenol, 5,5-dimethyl-1-pyrroline N-oxide (DMPO), ammonium chloride

(NH_4Cl), hexadecyl trimethyl ammonium bromide (CTAB) and activated carbon were purchased from Tianjin Xiensi Biochemical Technology Co., Ltd. Potassium nitrate (KNO_3), sulfuric acid (H_2SO_4) and ammonium hydroxide ($NH_3{\cdot}H_2O$) were acquired from Tianjin Damao Chemical Reagent Factory. Deuterium oxide (D_2O, 99.90 at.% D) was purchased from Shanghai Meiruier Biochemical Technology Co., Ltd. All chemicals were used as received without further purification.

Synthesis of BCNx and CN catalysts

The cyano-group-enriched and boron-doped BCNx nanotubes were synthesized via thermal condensation of a supramolecular precursor consisting of melamine-cyanuric acid modified with sodium cyanoborohydride[27,36]. Typically, melamine ($C_3H_6N_6$, 6.0 g, 47.57 mmol) was dissolved in 60 mL of distilled water and magnetically stirred for 30 min. The resultant suspension underwent hydrothermal treatment at a temperature of 180 °C for a duration of 24 h in a 100 mL Teflon-lined stainless-steel autoclave. Subsequently, the mixture was allowed to cool to ambient temperature and then isolated through centrifugation, followed by thorough washing and vacuum drying overnight at 60 °C. Thereafter, 100 mg of sodium cyanoborohydride ($NaBH_3CN$) was dispersed in 6 mL of distilled water, along with 2.0 g of the dried supramolecular precursor, and the mixture was stirred continuously for a period of 2 h. The final mixture was then subjected to vacuum drying overnight at 60 °C[61]. The obtained powder was uniformly spread in a 50 mL covered corundum porcelain boat and subjected to calcination under an Ar atmosphere with a heating rate of 5 °C min^{-1} to reach 550 °C, where the temperature was maintained for 4 h. The final material obtained was designated as BCNx. As a control experiment, a cyano-group-free and boron-free carbon nitride (CN) material was synthesized by directly calcining the supramolecular precursor without the addition of $NaBH_3$-CN.

Synthesis of Pd SA/BCNx and Pd SA/CN catalysts

Pd single-atom anchored BCNx and CN catalysts were synthesized via impregnation and thermal anchoring strategies. Typically, 100 mg of BCNx or CN was added to 10 mL of aqueous solution containing chloropalladic acid (H_2PdCl_6, 0.94 mM). The suspension was subjected to ultrasonication for 1 h, followed by stirring at room temperature for 4 h. Subsequently, the suspension was freeze-dried to obtain a solid powder. The resulting powder was uniformly spread in a 10 mL covered corundum porcelain boat and calcined under a N_2 atmosphere with a heating rate of 5 °C min^{-1} to reach 200 °C, where the temperature was maintained for 1 h. The final products were designated as Pd SA/BCNx and Pd SA/CN, with a Pd loading of 1 wt%. For comparison, Pt SA/BCNx, Au SA/BCNx, Ag SA/BCNx, Cu SA/BCNx, Co SA/BCNx and Fe SA/BCNx with metal loadings of 1 wt% were also synthesized using the same procedure.

Synthesis of Pd NP/BCNx catalysts

Pd nanoparticles were loaded onto BCNx by the chemical reduction method, with a theoretical loading amount of 1.0 wt% Pd. The specific process is as follows: 100 mg of BCNx was added to 10 mL of aqueous solution of chloropalladic acid (H_2PdCl_6, 0.94 mM). Subsequently, under stirring conditions, a certain amount of $NaBH_4$ solution (1 mol/L) was added at a Pd^{2+}: $NaBH_4$ molar ratio of 1:5. After reduction for 3 h, the precipitate was centrifuged and washed three times with deionized water and ethanol. The product was then dried overnight at 60 °C to obtain the Pd NP/BCNx catalyst.

Hydrolysis of PET powder and collection of EG solution

The hydrolysis of commercial PET powder (~80 mesh) was carried out in a 250 mL single-neck flask. First, 4.2 g of PET powder and 0.2 g of cetyltrimethylammonium bromide (CTAB, as a phase-transfer catalyst, 0.55 mmol) were added to 200 mL of 0.1 M NaOH aqueous solution. The reaction system was stirred at 500 rpm and heated to 60 °C to initiate the hydrolysis reaction. To maintain a constant pH in the reaction system, NaOH was continuously added dropwise until the PET was completely hydrolyzed, yielding equimolar amounts of terephthalic acid disodium salt (TPA-Na_2) and EG monomers. After the reaction, activated carbon was added to adsorb CTAB and other impurities in the solution. The mixture was then acidified and filtered to isolate the TPA monomer. After the filtrate was neutralized, the resulting solution was the EG-rich aqueous solution.

Photocatalytic C−N coupling for glycine production

Photocatalytic C−N coupling experiments were conducted in a 100 mL sealed glass reactor at room temperature and atmospheric pressure using a 300 W Xe lamp (MicroSolar300, Beijing Perfectlight Technology Co., Ltd., Supplementary Fig. 28). Typically, a certain amount of KNO_3 was dissolved in the aforementioned EG aqueous solution to prepare a mixed solution containing EG (C donor, 0.1 M) and KNO_3 (N donor, 0.5 M). The catalyst (20 mg) was dispersed in 50 mL of the EG/KNO_3 mixed solution. Prior to illumination, the reactor was purged with Ar for 30 min to remove residual gases, and then irradiated from the top of the reaction cell. After 24 h of illumination (320 nm < λ < 780 nm, 20 A Xe lamp current), the liquid phase products were analyzed via ^{1}H NMR spectroscopy.

Photocatalytic C−N coupling of g-scale (10 g) real-world post-consumer PET plastics

The photocatalytic C−N coupling of g-scale real-world post-consumer PET plastics was also evaluated under the same conditions, except that 4.2 g of PET powder was replaced with 10 g of commercial PET materials, including PET clothes (PET content >85%), PET bottles (PET content > 98%), PET bags (PET content > 90%), PET boxes (PET content > 85%) and PET towels (PET content > 60%). Furthermore, the photocatalytic C−N coupling reactions using different alcohols (methanol and glycerol) as carbon sources were also assessed under the same reaction conditions.

Characterization and analytical methods

The morphology and structure of the catalysts were characterized via various techniques. Transmission electron microscopy (TEM) images were acquired using a JEM-F200 field emission transmission electron microscope. High-angle angular dark field-scanning transmission electron microscopy (HAADF-STEM) images were acquired using a JEM-ARM200F transmission electron microscope equipped with a probe-corrector operating at 200 kV. X-ray absorption fine structure (XAFS) analysis was performed at the Pd *K*-edge at the BL14W beamline of the Shanghai Synchrotron Radiation Facility (SSRF). The X-ray beam was monochromatized using a Si(311) crystal monochromator. Pd *K*-edge extended X-ray absorption fine structure (EXAFS) spectra were recorded in transmission mode. The EXAFS data was processed using Athena to handle background corrections as well as to calibrate both the pre-edge and post-edge features. Following this, Fourier transform fitting was performed in Artemis. For the analysis of Pd SA/BCNx, k^3 weighting was utilized, with an R-range from 1 to 3 Å and a k-range set from 1.8 to 12 $Å^{-1}$[62].

X-ray Diffraction (XRD) analysis was conducted using a SmartLab X-ray diffractometer (3 kW) equipped with Cu-Kα radiation. Fourier transform infrared spectroscopy (FT-IR) was conducted using a Nicolet Magna 670 infrared spectrometer. X-ray photoelectron spectroscopy (XPS) was conducted on a Thermo Scientific ESCALAB 250Xi. Solid-state ^{11}B NMR spectra were recorded on an Agilent 600 M spectrometer. UV-vis diffuse reflectance spectra were obtained with a Varian Cary 500 Scan UV-vis spectrophotometer, using $BaSO_4$ as the reflectance standard. Photoluminescence (PL) and time-resolved photoluminescence (TR-PL) spectra were measured with an Edinburgh FLS1000 spectrophotometer. Transient photocurrent responses (TPR) and electrochemical impedance spectroscopy (EIS) were performed

on an AutoLab-302N electrochemical workstation, utilizing a standard three-electrode system, with the catalyst-coated FTO (1 × 1 cm²), Ag/AgCl, and Pt electrodes serving as the working, reference, and counter electrodes, respectively. High-resolution gas chromatograph–mass spectrometer (GC–MS) analysis was performed using a Thermo Fisher-Q Exactive Plus system. In situ XPS spectra were acquired with a Thermo Fisher-ESCALAB 250Xi. In situ electron spin resonance (ESR) data was recorded using a Bruker-EmxPlus spectrometer. In situ attenuated total reflection Fourier transform infrared spectroscopy (ATR-FTIR) was performed with a Thermo Fisher-iS50 spectrometer. Femtosecond transient absorption spectra of the photocatalysts were acquired using a pump–probe system (Helios, ultrafast system) equipped with a motorized optical delay line, allowing for time delays up to approximately 8 ns under ambient conditions. ^{1}H NMR spectra were recorded on a 400 MHz Bruker spectrometer (AVANCE III HD 400) with D_2O as the solvent and maleic acid (MA) as the internal standard. Quantitative analysis was performed via the following Eq. (1), and there are no products below the detection limit of the system.

$$n_{analyte} = \frac{S_{analyte}}{S_{standard}} \times \frac{2}{N_{monomer}} \times \frac{m_{standard}}{M_{standard}} \times \frac{V}{0.1} \quad (1)$$

The conversion of EG was calculated via the following Eq. (2).

$$Conversion = \frac{n_{analyte}}{n_0} \times 100\% \quad (2)$$

The integral areas of the peaks for the analyte and MA are denoted as $S_{analyte}$ and $S_{standard}$, respectively. The number of hydrogen atoms in the characteristic peak of the monomer used for quantitative analysis is represented by $N_{monomer}$. The mass and molar mass of MA are indicated by $m_{standard}$ and $M_{standard}$, respectively. V refers to the volume (50 mL) of the reaction mixture. n_0 and $n_{analyte}$ represent the initial total molar amount and after-reaction molar amount of EG, respectively.

Determination of NO_3^-RR products in C−N coupling reaction

The NO_3^-RR products were identified and quantified using UV-vis spectroscopy. The determination details of NO_2^- and NH_4^+ using UV-vis are discussed as follows. (a) NO_2^-: The testing solution was prepared by combining 2 mL of the diluted reaction mixture with 1.0 mL of sulfanilamide solution (0.01 g/L in 10% H_3PO_4) and 1.0 mL of N-(1-naphthyl) ethylenediamine dihydrochloride solution (0.01 g/L). The resulting mixture was allowed to react at room temperature for 20 min before being analyzed by UV-vis spectroscopy. Mechanism of NO_2^- detection: the reaction of NO_2^- with sulfanilamide in a phosphate medium to form a diazonium salt, which then undergoes coupling with N-(1-naphthyl)-ethylenediamine dihydrochloride to generate a red dye. The absorbance is measured at a wavelength of 540 nm. (b) NH_4^+: The quantification of NH_4^+ was performed using the indophenol blue method. After completing the reaction, 2.0 mL of the diluted electrolyte was mixed with a solution containing NaOH (1.0 M), salicylic acid (5.0 wt.%), sodium citrate (2.0 mL, 5.0 wt.%), and NaClO (1.0 mL, 0.05 M), followed by the addition of 0.20 mL of sodium nitroprusside solution (1.0 wt.%). The mixture was then allowed to stabilize for 2 h before UV-vis analysis. Mechanism of NH_4^+ detection: under alkaline conditions, NH_4^+ first reacts with NaClO to form NO_2^-, which then reacts with salicylic acid to produce $C_7H_5N_2O_3^-$. Finally, this compound undergoes coupling with sodium citrate and sodium nitroprusside to form an azo compound, which exhibits a specific absorbance peak at 651 nm.

DFT calculations

Spin-polarized periodic DFT calculations were performed via the Vienna ab initio simulation package (VASP, version 5.4.4)[63,64]. The electron-ion interaction was described via the projector augmented wave (PAW)[65,66]. The electron exchange and correlation energies were calculated based on the Perdew–Burke–Ernzerhof (PBE) functional[67], and the effects of van der Waals interactions were investigated based on Grimme's DFT-D3 method[68]. A plane-wave cut-off energy of 400 eV was applied for all DFT calculations.

For the model construction, a 2 × 2 anatase-TiO_2 (001) surface slab was established with twelve atomic layers (four O–Ti–O layers). The Pd single atom was embedded into the boron-doped C_3N_4 monolayer to simulate the Pd SA/BCN sample (Supplementary Data 1). During structure optimization, the six atomic layers on the bottom of the TiO_2 slab were fixed, while other atoms, including the adsorbates, were allowed to relax. For the Pd SA/BCN, relaxation was performed for all the atoms in the system. The structural relaxation was continued until the force on each atom was less than 0.02 eV/Å. The adsorption energy was defined as follows Eq. (3).

$$E_{ads} = E_{\frac{adsorbate}{slab}} - E_{adsorbate} - E_{slab} \quad (3)$$

where $E_{\frac{adsorbate}{slab}}$, $E_{adsorbate}$, and E_{slab} represent the total energies of the surface slab with the adsorbate, the isolated adsorbate species, and the optimized slab, respectively.

Data availability

The data that support the findings of this study are available within the article and Supplementary Information. Source data are provided with this paper or available from the corresponding author upon request.

References

1. Locasale, J. W. Serine, glycine and one-carbon units: cancer metabolism in full circle. *Nat. Rev. Cancer* **13**, 572–583 (2013).
2. Song, S. et al. Visible-light-driven amino acids production from biomass-based feedstocks over ultrathin CdS nanosheets. *Nat. Commun.* **11**, 4899 (2020).
3. Liao, L.-L. et al. α-Amino acids and peptides as bifunctional reagents: carbocarboxylation of activated alkenes via recycling CO_2. *J. Am. Chem. Soc.* **143**, 2812–2821 (2021).
4. Wang, W. W. et al. Glycine metabolism in animals and humans: implications for nutrition and health. *Amino Acids* **45**, 463–477 (2013).
5. Liao, P. S. et al. Cu-Bi bimetallic catalysts derived from metal-organic framework arrays on copper foam for efficient glycine electrosynthesis. *Angew. Chem. In. Ed.* **64**, e202417130 (2025).
6. Wu, R. R. et al. Enzymatic Electrosynthesis of Glycine from CO_2 and NH_3. *Angew. Chem. Int. Ed.* **62**, e202218387 (2023).
7. D'Este, M., Alvarado-Morales, M. & Angelidaki, I. Amino acids production focusing on fermentation technologies - A review. *Biotechnol. Adv.* **36**, 14–25 (2018).
8. Shao, J. et al. Amino acid electrosynthesis with oxygen vacancy-mediated CeO_2 nanocrystals: facet effect and catalytic mechanism. *JACS Au* **5**, 2015–2026 (2025).
9. Singh, S. K., Zhu, C., La Jeunesse, J., Fortenberry, R. C. & Kaiser, R. Experimental identification of aminomethanol (NH_2CH_2OH)-the key intermediate in the Strecker Synthesis. *Nat. Commun.* **13**, 375 (2022).
10. Li, P. F. & Zhang, B. B. Photocatalytic conversion of biomass and nitrate into glycine. *ACS Catal.* **14**, 18345–18353 (2024).
11. Li, P. F., Zhao, W. H., Wang, K. X., Wang, T. & Zhang, B. B. Photocatalytic synthesis of glycine from methanol and nitrate. *Angew. Chem. Int. Ed.* **63**, e202405370 (2024).
12. Li, X. et al. Photocatalytic C-N coupling from stable and transient intermediates for gram-scale acetamide synthesis. *Nat. Commun.* **16**, 3590 (2025).

13. Gao, J. Y. et al. Artificial photosynthesis of formamide via an oxidant-free photoinduced radical coupling route over Pt-CdS. *Angew. Chem. Int. Ed.* **64**, e202500747 (2025).
14. Han, Y. W., Ye, L., Gong, T. J. & Fu, Y. Surface-controlled CdS/Ti_3C_2 MXene schottky junction for highly selective and active photocatalytic dehydrogenation-reductive amination. *Angew. Chem. Int. Ed.* **62**, e202306305 (2023).
15. Rivas, M., del Valle, L. J., Turon, P., Alemán, C. & Puiggalí, J. Sustainable synthesis of amino acids by catalytic fixation of molecular dinitrogen and carbon dioxide. *Green Chem.* **20**, 685–693 (2018).
16. Dunn, W. W., Aikawa, Y. & Bard, A. J. Heterogeneous photosynthetic production of amino acids at platinum/titanium dioxide suspensions by near ultraviolet light. *J. Am. Chem. Soc.* **103**, 6893–6897 (1981).
17. Reiche, H. & Bard, A. J. Heterogeneous photosynthetic production of amino acids from methane-ammonia-water at platinum/titanium dioxide. Implications in chemical evolution. *J. Am. Chem. Soc.* **101**, 3127–3128 (1979).
18. Kang, H. X. et al. Mining the carbon intermediates in plastic waste upcycling for constructing C-S bond. *J. Am. Chem. Soc.* **146**, 18639–18649 (2024).
19. Li, W. L. et al. Atomic ruthenium-promoted cadmium sulfide for photocatalytic production of amino acids from biomass derivatives. *Angew. Chem. Int. Ed.* **63**, e202320014 (2024).
20. Li, J. et al. Heterogeneous electrosynthesis of C–N, C–S and C–P products using CO_2 as a building block. *Nat. Synth.* **3**, 809–824 (2024).
21. Liu, S. et al. Electrochemical lattice engineering of bismuthene for selective glycine synthesis. *Adv. Mater.* **37**, e2500843 (2025).
22. Xu, M. et al. Electrocatalytic and photocatalytic C-N coupling from small molecules. *Adv. Mater.* 2507144 https://doi.org/10.1002/adma.202507144 (2025).
23. Wan, Y., Zheng, M., Yan, W., Zhang, J. & Lv, R. Fundamentals and rational design of heterogeneous C-N coupling electrocatalysts for urea synthesis at ambient conditions. *Adv. Energy Mater.* **14**, 2303588 (2024).
24. Geyer, R., Jambeck, J. R. & Law, K. L. Production, use, and fate of all plastics ever made. *Sci. Adv.* **3**, e1700782 (2017).
25. Jambeck, J. R. et al. Plastic waste inputs from land into the ocean. *Science* **347**, 768–771 (2015).
26. Zhang, Z. et al. Recovering waste plastics using shape-selective nano-scale reactors as catalysts. *Nat. Sustain.* **2**, 39–42 (2019).
27. Tournier, V. et al. An engineered PET depolymerase to break down and recycle plastic bottles. *Nature* **580**, 216–219 (2020).
28. Yoshida, S. et al. A bacterium that degrades and assimilates poly(ethylene terephthalate). *Science* **351**, 1196–1199 (2016).
29. Yue, H. R., Zhao, Y. J., Ma, X. B. & Gong, J. L. Ethylene glycol: properties, synthesis, and applications. *Chem. Soc. Rev.* **41**, 4218–4244 (2012).
30. Li, M. & Zhang, S. B. Coupling waste plastic upgrading and CO_2 photoreduction to high-value chemicals by a binuclear Re-Ru heterogeneous catalyst. *ACS Catal.* **14**, 6717–6727 (2024).
31. Li, M. & Zhang, S. B. Tandem chemical depolymerization and photoreforming of waste PET plastic to high-value-added chemicals. *ACS Catal.* **14**, 2949–2958 (2024).
32. Ya, Z., Tang, L., Xu, D., Wang, H. & Zhang, S. B. Photoreforming of waste plastic by B-doped carbon nitride nanotube: Atomic-level modulation and mechanism insights. *AIChE J.* **71**, e18740 (2025).
33. Ya, Z., Zhang, S. B., Xu, D., Wang, H. & Li, M. Coupling plastic upgrading and photocatalysis: catalytic mechanisms and design principles. *ACS Catal.* **15**, 5339–5369 (2025).
34. Zhao, Z. Y., Yue, S., Yang, G. H., Wang, P. F. & Zhan, S. H. A unified view of carbon neutrality: solar-driven selective upcycling of waste plastics. *Tran. Tianjin Univ.* **30**, 1–26 (2024).
35. Liu, F. L. et al. Modulating adsorption behavior by single-site Pt on RuO_2 for efficient electrosynthesis of glycolic acid from plastic wastes. *Angew. Chem. Int. Ed.* **64**, e202422183 (2025).
36. Ya, Z., Li, M., Xu, D., Wang, H. & Zhang, S. B. Asymmetric atomic Pt-B dual-site catalyst for efficient photoreforming of waste polylactic acid plastics in seawater. *ACS Nano* **19**, 16011–16023 (2025).
37. Rao, P. et al. Single atomic cobalt electrocatalyst for efficient oxygen reduction reaction. *eScience* **2**, 399–404 (2022).
38. Wong, H. H. et al. Neighboring effect in single-atom catalysts for the electrochemical carbon dioxide reduction reaction. *eScience* **4**, 100140 (2024).
39. Gao, C. et al. Heterogeneous single-atom photocatalysts: fundamentals and applications. *Chem. Rev.* **120**, 12175–12216 (2020).
40. Jia, G. R., Zhang, Y. C., Yu, J. C. & Guo, Z. X. Asymmetric atomic dual-sites for photocatalytic CO_2 reduction. *Adv. Mater.* **36**, e2403153 (2024).
41. Liu, Y. et al. Selective synthesis of organonitrogen compounds via electrochemical C–N coupling on atomically dispersed catalysts. *ACS Nano* **18**, 23894–23911 (2024).
42. Hu, B. et al. Directing the C–N coupling pathway enables efficient urea electrosynthesis. *J. Am. Chem. Soc.* **147**, 21764–21777 (2025).
43. Tian, Y. et al. Thiophene-conjugated porous C_3N_4 nanosheets for boosted photocatalytic nicotinamide cofactor regeneration to facilitate solar-to-chemical enzymatic reactions. *Trans. Tianjin Univ.* **27**, 42–54 (2021).
44. Bai, Y., Li, S. J., Yin, B. L., Zhao, J. P. & Li, H. X. Visible light-induced photocatalysis: self-fenton degradation of p-ClPhOH over graphitic carbon nitride by a polyethylenimine bifunctional catalyst. *Trans. Tianjin Univ.* **30**, 130–139 (2024).
45. Yu, T., Liu, Z., Ma, J. & Tan, X. The photocatalytic oxidation of As(III) enhanced by surface alkalinized g-C_3N_4. *Trans. Tianjin Univ.* **26**, 40–48 (2020).
46. Wang, Z. Y. et al. Self-assembly synthesis of boron-doped graphitic carbon nitride hollow tubes for enhanced photocatalytic NOx removal under visible light. *Appl. Catal. B* **239**, 352–361 (2018).
47. Jeyalakshmi, V. et al. Pd single atoms on g-C_3N_4 photocatalysts: minimum loading for maximum activity. *Chem. Sci.* **16**, 4788–4795 (2025).
48. Hu, F. et al. Direct synthesis of atomically dispersed palladium atoms supported on graphitic carbon nitride for efficient selective hydrogenation reactions. *ACS Appl. Mater. Interfaces* **12**, 54146–54154 (2020).
49. Liu, G. M. et al. Single-atom Pd-N_3 sites on carbon-deficient g-C_3N_4 for photocatalytic H_2 evolution. *Trans. Tianjin Univ.* **27**, 139–146 (2021).
50. Zhao, D. M. et al. Synergy of dopants and defects in graphitic carbon nitride with exceptionally modulated band structures for efficient photocatalytic oxygen evolution. *Adv. Mater.* **31**, e1903545 (2019).
51. Jung, H. et al. Ultrathin Ti-deficient TiO_2 nanosheets with Pt single atoms enable efficient photocatalytic nitrate reduction to ammonia. *J. Am. Chem. Soc.* **147**, 9049–9055 (2025).
52. Jung, H., Kim, H., Will, J., Spiecker, E. & Schmuki, P. p-Type TiO_2 nanotubes: quantum confinement and Pt single atom decoration enable high selectivity photocatalytic nitrate reduction to ammonia. *Angew. Chem. Int. Ed.* **64**, e202415865 (2025).
53. Chen, H.-Y., Zhao, Z.-H., Huang, N.-Y., Huang, J.-R. & Liao, P.-Q. Rational design and synthesis of a metal–organic framework featuring Cu(I)–carbon bonds for enhanced artificial photosynthesis. *J. Am. Chem. Soc.* **147**, 38484–38491 (2025).
54. Chen, R. M. et al. Promoting the efficiency and selectivity of NO_3^- to-NH_3 reduction on Cu-O-Ti active sites via preferential glycol oxidation with holes. *Proc. Natl. Acad. Sci. USA* **120**, e2312550120 (2023).

55. Yu, S. S. et al. Accelerating the production of formate radicals for nitrate purification via a redox-regulated photocatalysis route. *Appl. Catal. B* **358**, 124419 (2024).
56. Zhang, R. et al. Phase engineering of high-entropy alloy for enhanced electrocatalytic nitrate reduction to ammonia. *Angew. Chem. Int. Ed.* **63**, e202407589 (2024).
57. Liang, G. F. et al. Production of primary amines by reductive amination of biomass-derived aldehydes/ketones. *Angew. Chem. Int. Ed.* **56**, 3050–3054 (2017).
58. Meng, X. et al. Selective oxidation of monoethanolamine to glycine over supported gold catalysts: The influence of support and the promoting effect of polyvinyl alcohol. *Mol. Catal.* **469**, 131–143 (2019).
59. Sun, X. et al. Unveiling the mechanism of thorough electrocatalytic oxidation of monoethanolamine by ultramicroelectrode and fast-scan cyclic voltammetry. *Electrochim. Acta.* **507**, 145095 (2024).
60. Pelckmans, M., Vermandel, W., Van Waes, F., Moonen, K. & Sels, B. F. Low-temperature reductive aminolysis of carbohydrates to diamines and aminoalcohols by heterogeneous catalysis. *Angew. Chem. Int. Ed.* **56**, 14540–14544 (2017).
61. Zhang, S. et al. Two-dimensional superlattice nanocatalysts unlock multimodal energy transformation-driven catalytic therapy. *Nat. Commun.* **16**, 5822 (2025).
62. Zeng, M. et al. ZSM-5-confined Cr1–O_4 active sites boost methane direct oxidation to C1 oxygenates under mild conditions. *EES Catal.* **1**, 153–161 (2023).
63. Kresse, G. & Furthmüller, J. Efficiency of ab-initio total energy calculations for metals and semiconductors using a plane-wave basis set. *Comput. Mater. Sci.* **6**, 15–50 (1996).
64. Kresse, G. & Furthmüller, J. Efficient iterative schemes for ab initio total-energy calculations using a plane-wave basis set. *Phys. Rev. B* **54**, 11169–11186 (1996).
65. Blöchl, P. E. Projector augmented-wave method. *Phys. Rev. B* **50**, 17953–17979 (1994).
66. Kresse, G. & Joubert, D. From ultrasoft pseudopotentials to the projector augmented-wave method. *Phys. Rev.* **59**, 1758–1775 (1999).
67. Perdew, J. P., Burke, K. & Ernzerhof, M. Generalized gradient approximation made simple. *Phys. Rev. Lett.* **77**, 3865–3868 (1996).
68. Grimme, S., Antony, J., Ehrlich, S. & Krieg, H. A consistent and accurate ab initio parametrization of density functional dispersion correction (DFT-D) for the 94 elements H-Pu. *J. Chem. Phys.* **132**, 154104 (2010).

Acknowledgements

This work was supported by the National Natural Science Foundation of China (22121004, J.L.G., 22178266, H.W., 22572141, S.Z.), Talent Program Fund of Tianjin University (0701321039, S.Z, 0903074107, S.Z), Postdoctoral Fellowship Program of CPSF under Grant Number GZC20240747, M.L.. This work was also supported by the Open Fund from the Key Laboratory of Advanced Energy Materials Chemistry, Ministry of Education (Nankai University). We acknowledge Tianjin University for their help in sample characterization.

Author contributions

J.L.G. and S.Z. conceptualized and supervised the work. J.L.G., S.Z., and H.W. designed the experiments. M.L., D.F., and Z.Y. performed the experiments and DFT calculations. J.L.G., S.Z., and Z.Y. wrote the paper. J.L.G., Z.Y., M.L., D.F., Y.Z., R.W, H.W., K.Z., D.X., Z.Z., X.Z., S.Y., H.W., and S.Z. contributed to the discussion of the research and approved the final version of the manuscript. Y.Z., M.L., and D.F. contributed equally.

Competing interests

The authors declare no competing interests.

Additional information

Supplementary information The online version contains supplementary material available at https://doi.org/10.1038/s41467-026-68666-z.

Correspondence and requests for materials should be addressed to Hua Wang, Shengbo Zhang or Jinlong Gong.

Peer review information *Nature Communications* thanks Biaobiao Zhang, Roberto Fiorenza and the other anonymous reviewer(s) for their contribution to the peer review of this work. A peer review file is available.